ELECTROMAGNETIC PIC SIMULATIONS WITH SMOOTH PARTICLES: A NUMERICAL STUDY

Martin Campos Pinto, Mathieu Lutz, Marie Mounier

Electromagnetic PIC simulations with smooth particles: a numerical study*

Martin Campos Pinto†, Mathieu Lutz‡and Marie Mounier§

June 24, 2015

Abstract

In this article we study a charge-conserving finite-element particle scheme for the Maxwell-Vlasov system that is based on a div-conforming representation of the electric field and we propose a high-order deposition algorithm for smooth particles with piecewise polynomial shape. The numerical performances of the method are assessed with an academic beam test-case, and it is shown that for an appropriate choice of the particle parameters the efficiency of the resulting method overcomes that of similar finite-element schemes using point particles.

Introduction

We consider a numerical scheme for the 2d Transverse Electric (TE) Maxwell system

$$\partial_t \boldsymbol{E} - c^2 \,\mathbf{curl}\, B = -\tfrac{1}{\varepsilon_0}\boldsymbol{J} \tag{1}$$

$$\partial_t B + \operatorname{curl} \boldsymbol{E} = 0 \tag{2}$$

coupled with a Vlasov equation to model the transport of particles with elementary charge q and mass m,

$$\partial_t f + \mathbf{v}\cdot\boldsymbol{\nabla}_{\mathbf{x}} f + \frac{q}{m}(\boldsymbol{E} + \mathbf{v}^\perp B)\cdot\boldsymbol{\nabla}_{\mathbf{v}} f = 0. \tag{3}$$

Here $f = f(t,\mathbf{x},\mathbf{v})$ is the plasma distribution function in phase-space, with $\mathbf{x} = (x,y)$ the position variable, $\mathbf{v} = (v_x, v_y)$ the velocity variable and $\mathbf{v}^\perp := (v_y, -v_x)$. In the above TE mode, the electromagnetic field takes the form $\boldsymbol{E} = (E_x(\mathbf{x},t), E_y(\mathbf{x},t))$, $B = B_z(\mathbf{x},t)$ and the 2d reduction yields two curl operators, namely

$$\mathbf{curl}\, B = (\partial_y B, -\partial_x B) \qquad \text{and} \qquad \operatorname{curl} \boldsymbol{E} = \partial_x E_y - \partial_y E_x.$$

Finally the charge and the current density are given by

$$\rho(t,\mathbf{x}) := q\int_{\mathbb{R}^2} f(t,\mathbf{x},\mathbf{v})\,\mathrm{d}\mathbf{v}, \tag{4}$$

$$\boldsymbol{J}(t,\mathbf{x}) := q\int_{\mathbb{R}^2} \mathbf{v} f(t,\mathbf{x},\mathbf{v})\,\mathrm{d}\mathbf{v} \tag{5}$$

*An important part of this work was carried out in the Congapic project during the Cemracs 14 research session, with funding support from the AMIES agency.

†CNRS, UMR 7598, Laboratoire Jacques-Louis Lions, F-75005, Paris, France

‡Université de Toulouse, UMR5219, Institut de Mathématiques de Toulouse, F-31062 Toulouse, France

§Nuclétudes, CS 70117, 91978 Courtaboeuf cedex, France

and we recall that they satisfy a continuity equation

$$\partial_t \rho + \operatorname{div} \boldsymbol{J} = 0. \tag{6}$$

As is well known and formally verified by taking the divergence of the Ampère equation (1), this property of the source guarantees that the solutions of the above Maxwell evolution system satisfy the Gauss law

$$\operatorname{div} \boldsymbol{E} = \tfrac{1}{\varepsilon_0}\rho \tag{7}$$

at any time t, as long as it is the case for the initial solution $\boldsymbol{E}^0$. (For the magnetic field the Gauss law is degenerate since $B = B_z(\mathbf{x}, t)$ has a zero divergence by construction.) The aim of this article is to describe a FEM-PIC scheme with smooth particles for the above Maxwell-Vlasov system that is charge-conserving in the sense that it preserves a (strong) Gauss law for the numerical solution, and to study its numerical performances with an academic beam test-case.

The outline is as follows. In Section 1 we describe a mixed finite-element method for the time-dependent Maxwell system (1)-(2) that is based on a div-conforming representation of the electric field $\boldsymbol{E}$, and we recall the particle approximation of the Vlasov equation (3). In this charge-conserving scheme the current is discretized using a Raviart-Thomas interpolation that is recalled in Section 2.1, and in Sections 2.2 and 2.3 we describe how to apply it using numerical Fekete quadratures in the case where $\boldsymbol{J}$ is approximated by smooth particles. Finally we show in Section 3 some numerical results obtained for a smooth electron beam in a simple domain. In particular, we discuss how the accuracy and efficiency of the resulting FEM-PIC scheme vary with some parameters of the smooth particles, and we compare it with two FEM-PIC methods using point particles.

1 Description of the numerical scheme

In the present Section we describe the numerical method used to simulate the Maxwell-Vlasov system. We consider a bounded computational domain Ω with Lipschitz boundary that is partitioned by a regular family of conforming simplicial meshes $(\mathcal{T}_h)_{h>0}$, and inside each triangle $T \in \mathcal{T}_h$ we assume that the vertices $\{\mathbf{x}_0^T, \mathbf{x}_1^T, \mathbf{x}_2^T\}$ are numbered counterclockwise. We denote the corresponding edges by $\mathcal{E}(T) = \{e_0^T, e_1^T, e_2^T\}$, so that e_i^T and $\mathbf{x}_i^T$ are opposite. We also let $\boldsymbol{n}_e^T$ be the outward unit vector of T that is normal to e, and $\boldsymbol{\tau}_e^T$ the associated tangent vector obtained by rotating $\boldsymbol{n}_e^T$ through + 90 degrees. We then write $\mathcal{E}_h = \cup_{T\in\mathcal{T}_h}\mathcal{E}(T)$ and assuming that the triangles are given arbitrary indices, we fix an orientation for the edges as follows. For any $e \in \mathcal{E}_h$, we let $T^-(e)$ be the triangle of minimum index for which e is an edge. If e is shared by another triangle we denote the latter by $T^+(e)$. Note that, due to the conformity of the mesh, no more than 2 triangles can have e as an edge. The edge e is then oriented by setting

$$\mathbf{x}_0^e := \mathbf{x}_{i+1}^{T^-(e)}, \quad \mathbf{x}_1^e := \mathbf{x}_{i+2}^{T^-(e)} \qquad \text{where } i \text{ is such that } e = e_i^{T^-(e)} \tag{8}$$

(and where for simplicity we have identified $\mathbf{x}_i^{T^-(e)}$ and $\mathbf{x}_{i+3}^{T^-(e)}$). We also set

$$\boldsymbol{n}_e := \boldsymbol{n}_e^{T^-(e)},$$

and observe that if e is an interior edge then we have $\boldsymbol{n}_e = -\boldsymbol{n}_e^{T^+(e)}$. We denote by $\hat{T}$ a reference triangle with vertices

$$\hat{\mathbf{x}}_0 := \begin{pmatrix} 0 \\ 0 \end{pmatrix}, \quad \hat{\mathbf{x}}_1 := \begin{pmatrix} 1 \\ 0 \end{pmatrix}, \quad \hat{\mathbf{x}}_2 := \begin{pmatrix} 0 \\ 1 \end{pmatrix}$$

and we let

$$F_T : \hat{T} \to T, \quad \hat{\mathbf{x}} \mapsto \mathbf{x}_0^T + \mathbf{F}_T \hat{\mathbf{x}}, \qquad \mathbf{F}_T := \begin{pmatrix} x_1^T - x_0^T & x_2^T - x_0^T \\ y_1^T - y_0^T & y_2^T - y_0^T \end{pmatrix} \tag{9}$$

be the affine function that maps $\hat{T}$ on any $T \in \mathcal{T}_h$ (and preserves the numbering of the vertices). As for the boundary conditions, we will consider standard metallic and Silver-Müller boundary conditions, namely

$$\boldsymbol{E} \times \boldsymbol{n} = \begin{cases} 0 & \text{on the metallic boundaries} \quad \Gamma_M \subset \partial\Omega \\ c(B \times \boldsymbol{n}) \times \boldsymbol{n} = -cB & \text{on the absorbing boundaries} \quad \Gamma_A = \partial\Omega \setminus \Gamma_M \end{cases} \tag{10}$$

where $\boldsymbol{n}$ is the outward unit vector normal to $\partial\Omega$.

1.1 Finite element scheme for the Maxwell system

For the Maxwell system we consider a space discretization that relies on a mixed formulation with a strong Ampère equation. It involves a continuous finite-element space for the magnetic field

$$V_h^\mu := \mathbb{P}_p(\mathcal{T}_h) \cap H(\mathbf{curl}; \Omega) = \{u \in \mathcal{C}(\Omega) : u|_T \in \mathbb{P}_p(T),\ T \in \mathcal{T}_h\} \tag{11}$$

where $\mathbb{P}_p(T)$ denotes the space of polynomials of total degree $\leq p$ on T, and a div-conforming Raviart-Thomas finite-element space for the electric field

$$V_h^\varepsilon := \mathcal{RT}_{p-1}(\Omega, \mathcal{T}_h) = \{\boldsymbol{u} \in H(\mathrm{div}; \Omega) : \boldsymbol{u}|_T \in \mathcal{RT}_{p-1}(T),\ T \in \mathcal{T}_h\} \tag{12}$$

with $\mathcal{RT}_{p-1}(T) := \mathbb{P}_{p-1}(T)^2 + \binom{x}{y}\mathbb{P}_{p-1}(T)$ see e.g. [3, 1] for further details on $H(\mathrm{div})$ conforming spaces. Here the exponents μ and ε stand for "magnetic" and "electric" respectively. In a semi-discrete setting, the approximate electro-magnetic field is then defined as the solution $(B_h(t), \boldsymbol{E}_h(t)) \in V_h^\mu \times V_h^\varepsilon$ to the system

$$\begin{cases} \langle \partial_t B_h, \varphi \rangle + \langle \boldsymbol{E}_h, \mathbf{curl}\, \varphi \rangle + c\langle B_h, \varphi \rangle_{\Gamma_A} = 0 & \varphi \in V_h^\mu \subset H(\mathbf{curl}; \Omega) = H^1(\Omega) \\ \langle \partial_t \boldsymbol{E}_h, \boldsymbol{\varphi} \rangle - c^2 \langle \mathbf{curl}\, B_h, \boldsymbol{\varphi} \rangle = -\frac{1}{\varepsilon_0} \langle \boldsymbol{J}_h, \boldsymbol{\varphi} \rangle & \boldsymbol{\varphi} \in V_h^\varepsilon \subset H(\mathrm{div}; \Omega) \end{cases} \tag{13}$$

where $\boldsymbol{J}_h \in V_h^\varepsilon$ is an approximate current density. This discretization is of course not new. Its convergence is established in [6] (for the 3d Maxwell system) and its charge conservation properties are advocated in [7], where it is presented as a "D/H formulation" due to the fact that it essentially relies on representing the electric field (and the current density) as a 2-form defined through its fluxes.

This discretization has several interesting properties. First, using the embedding $\mathbf{curl}\, V_h^\mu \subset V_h^\varepsilon$ we see that the discrete Ampère equation holds in a strong (i.e., pointwise) sense in V_h^ε

$$\partial_t \boldsymbol{E}_h - c^2\, \mathbf{curl}\, B_h = -\tfrac{1}{\varepsilon_0} \boldsymbol{J}_h. \tag{14}$$

Second, we observe that if $\boldsymbol{J}_h$ is defined as

$$\boldsymbol{J}_h := \pi_h^{\mathrm{div}} \boldsymbol{J} \tag{15}$$

where π_h^{div} is the finite-element interpolation on the Raviart-Thomas space V_h^ε (see Section 2), then the approximate electric field satisfies a (strong, i.e., pointwise) Gauss law involving an approximate charge density. Indeed, as can be verified with integrations by parts, the finite-element interpolation satisfies a commuting diagram property

$$\mathrm{div}\, \pi_h^{\mathrm{div}} \boldsymbol{u} = P_h\, \mathrm{div}\, \boldsymbol{u}, \qquad \boldsymbol{u} \in H^1(\Omega) \tag{16}$$

where $P_h : L^2(\Omega) \to \mathbb{P}_{p-1}(\mathcal{T}_h)$ is the L^2-projection on the piecewise polynomials of degree $\leq p$, i.e.,

$$\langle P_h u, \varphi \rangle = \langle u, \varphi \rangle, \qquad \varphi \in \mathbb{P}_{p-1}(\mathcal{T}_h).$$

In particular, taking the divergence of the strong Ampère equation (14) and using the continuity equation (6) yields

$$\operatorname{div} \boldsymbol{E}_h = \frac{1}{\varepsilon_0} \rho_h$$

with an approximate charge density $\rho_h = P_h \rho$.

Remark 1.1. *We observe that the electric field $\boldsymbol{E}_h$ can be computed in a discontinuous space $\tilde{V}_h^\varepsilon$ containing V_h^ε, indeed the discrete Ampère equation holds in a strong (i.e., pointwise) sense, so that the electric field $\boldsymbol{E}_h$ will belong to the* div*-conforming Raviart-Thomas space V_h^ε as long as its initial value $\boldsymbol{E}_h$ does so.*

Remark 1.2. *A probably more usual finite-element discretization of the TE Maxwell system* (1)-(2) *consists of looking for $\boldsymbol{E}_h(t)$ in a curl-conforming space V_h^ε and $B_h(t)$ in a space V_h^μ containing* $\operatorname{curl} V_h^\varepsilon$*, such that*

$$\begin{cases} \langle \partial_t \boldsymbol{E}_h, \boldsymbol{\varphi} \rangle - c^2 \langle B_h, \operatorname{curl} \boldsymbol{\varphi} \rangle + c \langle \boldsymbol{n} \times \boldsymbol{E}_h, \boldsymbol{n} \times \boldsymbol{\varphi} \rangle_{\Gamma_A} = -\frac{1}{\varepsilon_0} \langle \boldsymbol{J}_h, \boldsymbol{\varphi} \rangle & \boldsymbol{\varphi} \in V_h^\varepsilon \subset H(\operatorname{curl}; \Omega) \\ \langle \partial_t B_h, \varphi \rangle + \langle \operatorname{curl} \boldsymbol{E}_h, \varphi \rangle = 0 & \varphi \in V_h^\mu \subset L^2(\Omega). \end{cases} \tag{17}$$

Compared to (13)*, an explicit time discretization based on* (17) *leads to inverting at each time step a mass matrix in a curl-conforming space (for $\boldsymbol{E}_h$) instead of a* **curl***-conforming space (for B_h). Because the former consists of vector-valued fields, it results in more expensive solves.*

1.2 Particle method for the Vlasov equation

The Vlasov equation (3) is discretized by a particle method which consists of approximating f by a collection of N numerical particles,

$$f_N(t, \mathbf{x}, \mathbf{v}) := \sum_{k=1}^{N} w_k S(\mathbf{x} - \mathbf{x}_k(t)) S(\mathbf{v} - \mathbf{v}_k(t)). \tag{18}$$

Here the shape function S can either be a Dirac measure or a smooth, symmetric function ($S(-\mathbf{v}) = S(\mathbf{v})$) with compact support and unit integral. As for the phase-space particle centers $(\mathbf{x}_k, \mathbf{v}_k)$, they are initialized together with the particle weights w_k in such a way that $f_N(t = 0)$ approximates the initial data f^0 in a function or in a measure's sense, and they are transported by following the characteristic curves associated to (3), i.e.,

$$\begin{cases} \dfrac{\mathrm{d}\mathbf{x}_k}{\mathrm{d}t} = \mathbf{v}_k \\ \dfrac{\mathrm{d}\mathbf{v}_k}{\mathrm{d}t} = \dfrac{q}{m} \Big(\boldsymbol{E}(\mathbf{x}_k, t) + \mathbf{v}_k^\perp B(\mathbf{x}_k, t) \Big). \end{cases} \tag{19}$$

Accordingly, we can define a current and a charge density from the above particle approximation, namely

$$\begin{cases} \rho_N(t, \mathbf{x}) := q \displaystyle\int_{\mathbb{R}^2} f_N(t, \mathbf{x}, \mathbf{v}) \, \mathrm{d}\mathbf{v} = q \sum_{k=1}^{N} w_k S(\mathbf{x} - \mathbf{x}_k(t)) \\ \boldsymbol{J}_N(t, \mathbf{x}) := q \displaystyle\int_{\mathbb{R}^2} \mathbf{v} f_N(t, \mathbf{x}, \mathbf{v}) \, \mathrm{d}\mathbf{v} = q \sum_{k=1}^{N} w_k \mathbf{v}_k(t) S(\mathbf{x} - \mathbf{x}_k(t)) \end{cases} \tag{20}$$

where we have used the symmetry of S in the last equality.

The coupling between the Vlasov and the Maxwell discretizations is then essentially carried out by using the discrete fields $\boldsymbol{E}_h$, B_h in the above ODE, and by setting $\boldsymbol{J} = \boldsymbol{J}_N$ in the finite element scheme (13)-(15).

1.3 Fully discrete FEM-PIC scheme

For computational issues it will be more convenient to represent the electric field $\boldsymbol{E}_h$ in a fully discontinuous space $\tilde{V}_h^\varepsilon$ which contains the div-conforming space V_h^ε, see Remark 1.1. Let us denote by

$$\sigma_\lambda^\mu, \quad \lambda \in \Lambda_h^\mu \qquad \text{and} \qquad \tilde{\sigma}_\lambda^\varepsilon, \quad \lambda \in \tilde{\Lambda}_h^\varepsilon$$

two bases of degrees of freedom for the respective spaces V_h^μ and $\tilde{V}_h^\varepsilon$, with Λ_h^μ and $\tilde{\Lambda}_h^\varepsilon$ appropriate sets of indices or multi-indices. We next denote by

$$\varphi_\lambda^\mu, \quad \lambda \in \Lambda_h^\mu \qquad \text{and} \qquad \tilde{\boldsymbol{\varphi}}_\lambda^\varepsilon, \quad \lambda \in \tilde{\Lambda}_h^\varepsilon \tag{21}$$

the associate bases for the spaces themselves, that are bi-orthogonal to the above degrees of freedom in the sense that

$$\sigma_\lambda^\mu(\varphi_\gamma^\mu) = \delta_{\lambda,\gamma} \qquad \text{and} \qquad \tilde{\sigma}_\lambda^\varepsilon(\tilde{\boldsymbol{\varphi}}_\gamma^\varepsilon) = \delta_{\lambda,\gamma}$$

holds for all λ and γ in Λ_h^μ and $\tilde{\Lambda}_h^\varepsilon$, respectively. In the same way we could define a basis for the div-conforming space V_h^ε: this will be done explicitely in Section 2.1 below. Then, introducing the matrices

$$\begin{gathered}\mathbf{M}^\mu = \Big(\langle \varphi_\lambda^\mu, \varphi_\gamma^\mu\rangle\Big)_{\lambda,\gamma\in\Lambda_h^\mu}, \quad \tilde{\mathbf{M}}^\varepsilon = \Big(\langle \tilde{\boldsymbol{\varphi}}_\lambda^\varepsilon, \tilde{\boldsymbol{\varphi}}_\gamma^\varepsilon\rangle\Big)_{\lambda,\gamma\in\tilde{\Lambda}_h^\varepsilon}, \quad \tilde{\mathbf{C}}^\varepsilon = \Big(\tilde{\sigma}_\lambda^\varepsilon(\mathbf{curl}\,\varphi_\gamma^\mu)\Big)_{(\lambda,\gamma)\in\tilde{\Lambda}_h^\varepsilon\times\Lambda_h^\mu},\\ \text{and} \quad \mathbf{A}^\mu = \Big(\langle \varphi_\lambda^\mu, \varphi_\gamma^\mu\rangle_{\Gamma_A}\Big)_{\lambda,\gamma\in\Lambda_h^\mu},\end{gathered} \tag{22}$$

and the column vectors corresponding to the fields and the current density

$$\mathbf{B} = \big(\sigma_\lambda^\mu(B_h)\big)_{\lambda\in\Lambda_h^\mu}, \quad \tilde{\mathbf{E}} = \big(\tilde{\sigma}_\lambda^\varepsilon(\boldsymbol{E}_h)\big)_{\lambda\in\tilde{\Lambda}_h^\varepsilon}, \qquad \text{and} \qquad \tilde{\mathbf{J}} = \big(\tilde{\sigma}_\lambda^\varepsilon(\pi_h^{\mathrm{div}}\boldsymbol{J})\big)_{\lambda\in\tilde{\Lambda}_h^\varepsilon}, \tag{23}$$

the conforming method (13) reads:

$$\begin{aligned}\tfrac{\mathrm{d}}{\mathrm{d}t}\mathbf{M}^\mu\mathbf{B} + (\tilde{\mathbf{C}}^\varepsilon)^t\tilde{\mathbf{M}}^\varepsilon\tilde{\mathbf{E}} + c\mathbf{A}^\mu\mathbf{B} &= 0\\ \tfrac{\mathrm{d}}{\mathrm{d}t}\tilde{\mathbf{E}} - c^2\tilde{\mathbf{C}}^\varepsilon\mathbf{B} &= -\tfrac{1}{\varepsilon_0}\tilde{\mathbf{J}}.\end{aligned} \tag{24}$$

A leap-frog time stepping with implicit treatment of the absorbing boundary conditions on Γ_A leads then to the following fully discrete scheme

$$\begin{aligned}\mathbf{M}^\mu\mathbf{B}^{n+\frac12} &= \mathbf{M}^\mu\boldsymbol{B}^{n-\frac12} - \Delta t\big((\tilde{\mathbf{C}}^\varepsilon)^t\tilde{\mathbf{M}}^\varepsilon\tilde{\mathbf{E}}^n + c\mathbf{A}^\mu\mathbf{B}^{n+\frac12}\big),\\ \tilde{\mathbf{E}}^{n+1} &= \tilde{\mathbf{E}}^n + \Delta t\big(c^2\tilde{\mathbf{C}}^\varepsilon\mathbf{B}^{n+\frac12} - \tfrac{1}{\varepsilon_0}\tilde{\mathbf{J}}^{n+\frac12}\big).\end{aligned} \tag{25}$$

Remark 1.3. *Of course, in order that* (22) *and* (23) *indeed define* matrices *and* vectors*, we need to use indexing functions for the sets Λ_h^μ and $\tilde{\Lambda}_h^\varepsilon$. We assume that these we are given.*

Now, because in practice the characteristic curves (19) are advanced with the leap-frog scheme

$$\begin{cases}\mathbf{x}_k^{n+1} = \mathbf{x}_k^n + \Delta t\mathbf{v}_k^{n+\frac12},\\ \mathbf{v}_k^{n+\frac12} = \mathbf{v}_k^{n-\frac12} + \dfrac{q\Delta t}{m}\left(\boldsymbol{E}_h^n(\mathbf{x}_k^n) + \left(\dfrac{\mathbf{v}_k^{n+\frac12} - \mathbf{v}_k^{n-\frac12}}{2}\right)^\perp B_h^n(\mathbf{x}_k^n)\right),\end{cases} \tag{26}$$

we need to compute the B_h field on the integer time steps. Thus, we decompose the Faraday equation in two half-time steps. Using again an implicit treatment of the absorbing boundary terms we obtain

$$\begin{aligned}(\mathbf{M}^\mu + c\tfrac{\Delta t}{2}\mathbf{A}^\mu)\mathbf{B}^n &= \mathbf{M}^\mu\mathbf{B}^{n-\frac12} - \tfrac{\Delta t}{2}(\tilde{\mathbf{C}}^\varepsilon)^t\tilde{\mathbf{M}}^\varepsilon\tilde{\mathbf{E}}^n\\ (\mathbf{M}^\mu + c\tfrac{\Delta t}{2}\mathbf{A}^\mu)\mathbf{B}^{n+\frac12} &= \mathbf{M}^\mu\mathbf{B}^n - \tfrac{\Delta t}{2}(\tilde{\mathbf{C}}^\varepsilon)^t\tilde{\mathbf{M}}^\varepsilon\tilde{\mathbf{E}}^n\\ \tilde{\mathbf{E}}^{n+1} &= \tilde{\mathbf{E}}^n + \Delta t\big(c^2\tilde{\mathbf{C}}^\varepsilon\mathbf{B}^{n+\frac12} - \tfrac{1}{\varepsilon_0}\tilde{\mathbf{J}}^{n+\frac12}\big).\end{aligned} \tag{27}$$

Note that since here the entries of the column vectors $\mathbf{B}^n$ and $\tilde{\mathbf{E}}^n$ represent coefficients in the bases (21), the discrete fields $\boldsymbol{E}_h^n$ and B_h^n can be evaluated on any $\mathbf{x}\in\Omega$ with

$$B_h^n(\mathbf{x}) = \sum_{\lambda\in\Lambda_h^\mu}(\mathbf{B}^n)_\lambda\varphi_\lambda^\mu(\mathbf{x}) \qquad\text{and}\qquad \boldsymbol{E}_h^n(\mathbf{x}) = \sum_{\lambda\in\tilde\Lambda_h^\varepsilon}(\tilde{\mathbf{E}}^n)_\lambda\tilde{\boldsymbol{\varphi}}_\lambda^\varepsilon(\mathbf{x}).$$

The procedure to compute $\tilde{\mathbf{J}}^{n+\frac12}$ from the particle distribution will be explained in the following sections.

2 The Raviart-Thomas current deposition

2.1 Interpolation on Raviart-Thomas finite elements

On the (local) Raviart-Thomas space $\mathcal{RT}_{p-1}(T)$ (see Section 1.1) associated with some aribtrary $T\in\mathcal{T}_h$, we recall that the classical degrees of freedom (see, e.g., [3] or [1, Sec. 2.3.1 and Ex. 2.5.3]) correspond to spaces of linear forms given by

$$\begin{cases}\mathcal{M}_T^\varepsilon(\boldsymbol{u}) := \{\int_T \boldsymbol{u}\cdot\pi \ :\ \pi\in\mathbb{P}_{p-2}(T)^2\}\\ \mathcal{M}_e^\varepsilon(\boldsymbol{u}) := \{\int_e(\boldsymbol{u}\cdot\boldsymbol{n}_e)\,\pi \ :\ \pi\in\mathbb{P}_{p-1}(e)\} \qquad \text{for every edge } e\in\mathcal{E}(T).\end{cases} \tag{28}$$

As is well known these degrees of freedom are unisolvent and $H(\mathrm{div})$-conforming. Now, to compute the Raviart-Thomas projection of a current density one needs to specify a basis of degrees of freedom, i.e., a particular set of linear forms that span the above spaces $\mathcal{M}_T^\varepsilon(\boldsymbol{u})$ and $\mathcal{M}_e^\varepsilon(\boldsymbol{u})$ for any (smooth) function $\boldsymbol{u}$. Here we shall use bases of $\mathbb{P}_q(T)$ and $\mathbb{P}_q(e)$ made of Bernstein polynomials. We recall that given a multi-index α in $\mathbb{N}^3$, resp. $\mathbb{N}^2$, the associated Bernstein polynomial on the triangle T, resp. edge e is defined by

$$\pi_{T,\alpha} := (\lambda_0^T)^{\alpha_0}(\lambda_1^T)^{\alpha_1}(\lambda_2^T)^{\alpha_2} \quad\text{for}\quad \alpha\in\mathbb{N}^3 \qquad\text{resp.}\qquad \pi_{e,\alpha} := (\lambda_0^e)^{\alpha_0}(\lambda_1^e)^{\alpha_1} \quad\text{for}\quad \alpha\in\mathbb{N}^2, \tag{29}$$

where λ_i^T, resp. λ_i^e, is the i-th barycentric coordinate of T, resp. e (i.e., the affine function which values are 1 on $\mathbf{x}_i^T$, resp. $\mathbf{x}_i^e$, and 0 on the other vertices). As is well known, bases of $\mathbb{P}_q(T)$ and $\mathbb{P}_q(e)$ are then given by the collections $\{\pi_{T,\alpha}:\alpha\in\Gamma_q^2\}$ and $\{\pi_{e,\alpha}:\alpha\in\Gamma_q^1\}$, where the sets Γ_q^d contain the multi-indices of length $d+1$ and weight q, i.e.,

$$\Gamma_q^d := \{\alpha=(\alpha_0,\dots,\alpha_d)\in\mathbb{N}^{d+1} :\ \alpha_0+\cdots+\alpha_d = q\},$$

Using these bases we consider the following degrees of freedom:

$$\begin{cases}\sigma_{T,d,\alpha}^\varepsilon(\boldsymbol{u}) := |\mathbf{F}_T|^{-1}\int_T(\tilde{\mathbf{F}}_T^t\boldsymbol{u})_d\,\pi_{T,\alpha} & \text{for } T\in\mathcal{T}_h,\ \ d=0,1,\ \ \alpha\in\Gamma_{p-2}^2\\ \sigma_{e,\beta}^\varepsilon(\boldsymbol{u}) := \int_e(\boldsymbol{u}\cdot\boldsymbol{n}_e)\,\pi_{e,\beta} & \text{for } e\in\mathcal{E}_h,\ \ \beta\in\Gamma_{p-1}^1,\end{cases} \tag{30}$$

where $\mathbf{F}_T$ is defined in (9) and $\tilde{\mathbf{F}}_T := \mathbf{R}\mathbf{F}_T\mathbf{R}^t$ is derived from $\mathbf{F}_T$ by the rotation $\mathbf{R} := \left(\begin{smallmatrix}0 & 1\\ -1 & 0\end{smallmatrix}\right)$ Accordingly, we denote the sets of multi-indices for the degrees of freedom by

$$\Lambda_h^\varepsilon := \Lambda_{h,\mathrm{vol}}^\varepsilon\cup\Lambda_{h,\mathrm{edge}}^\varepsilon \quad\text{with}\quad \begin{cases}\Lambda_{h,\mathrm{vol}}^\varepsilon := \mathcal{T}_h\times\{0,1\}\times\Gamma_{p-2}^2\\ \Lambda_{h,\mathrm{edge}}^\varepsilon := \mathcal{E}_h\times\Gamma_{p-1}^1.\end{cases} \tag{31}$$

The corresponding finite element interpolation on $V_h^\varepsilon := \mathcal{RT}_{p-1}(\mathcal{T}_h;\Omega)$, that we denote

$$\pi_h^{\mathrm{div}} : H^1(\Omega) \to V_h^\varepsilon,$$

is then obtained by stitching together local projectors π_T^{div} on $\mathcal{RT}_{p-1}(T)$ which are defined by the relations

$$\mathcal{M}_T^\varepsilon(\pi_T^{\mathrm{div}}\boldsymbol{u} - \boldsymbol{u}) = \{0\}, \quad \mathcal{M}_e^\varepsilon(\pi_T^{\mathrm{div}}\boldsymbol{u} - \boldsymbol{u}) = \{0\}, \qquad e \in \mathcal{E}(T), \tag{32}$$

in the sense that $\pi_h^{\mathrm{div}}\boldsymbol{u} := \sum_{T\in\mathcal{T}_h} \pi_T^{\mathrm{div}}\boldsymbol{u}$. We can verify that this amounts to computing the approximate current density $\boldsymbol{J}_h = \pi_h^{\mathrm{div}}(\boldsymbol{J})$ from (15) with

$$\boldsymbol{J}_h = \sum_{\lambda\in\Lambda_h^\varepsilon} \sigma_\lambda^\varepsilon(\boldsymbol{J})\boldsymbol{\varphi}_\lambda^\varepsilon. \tag{33}$$

It then remains to compute approximations of the above degrees of freedom in the case where $\boldsymbol{J}$ is defined through the moving particles. These approximations will be established in the next Sections.

2.2 Smooth particle current deposition with numerical quadratures

Since a discrete version of the continuity equation (6) can be obtained in particle schemes by averaging the time-dependent current density (20) over the time step, and evaluating the charge density at t_n (see [2] and the reference therein), we consider the following smoothed, time-averaged current density:

$$\boldsymbol{J}_N^{n+\frac{1}{2}}(\mathbf{x}) := \int_{t_n}^{t_{n+1}} \boldsymbol{J}_N(t,\mathbf{x})\frac{\mathrm{d}t}{\Delta t} = q\sum_{k=1}^N w_k \int_{t_n}^{t_{n+1}} \mathbf{v}_k^{n+1/2} S(\mathbf{x}-\mathbf{x}_k(t))\frac{\mathrm{d}t}{\Delta t}. \tag{34}$$

Here the characteristic trajectories can be taken piecewise affine, $\mathbf{x}_k(t) := \mathbf{x}_k^n + \mathbf{v}_k^{n+\frac{1}{2}}(t-t_n)$ with constant speeds on $[t_n, t_{n+1}]$, updated with (26). As for S we choose a tensor-product shape function with univariate degree $2a$, $a \in \mathbb{N}$, and radius $\epsilon > 0$, derived from the one proposed by Jacobs and Hesthaven in [4], i.e.,

$$S(\mathbf{x}) = S_\epsilon(\mathbf{x}) := S_\epsilon^{1d}(x)S_\epsilon^{1d}(y) \quad \text{with} \quad S_\epsilon^{1d}(s) := \begin{cases} \frac{c_a}{\epsilon}\left[1-\left(\frac{s}{\epsilon}\right)^2\right]^a & \text{if } s\in[-\epsilon,\epsilon] \\ 0 & \text{otherwise,} \end{cases} \tag{35}$$

where $c_a := 1/(2W(2a+1))$ and $W(m) := \int_0^{\frac{\pi}{2}} \cos(\theta)^m \,\mathrm{d}\theta$ is the standard Wallis integral. To deposit the current carried by the smooth particles in the $H(\mathrm{div})$-conforming space V_h^ε we will approximate the values of the coefficients in (33) with quadrature formulas. To this aim we use triangular Fekete points of degree $q \in 3\mathbb{N}$ computed in Ref. [8]. On every triangle T they provide a quadrature formula

$$\int_T u \approx \sum_{j=1}^{N_{\mathrm{vol}}} w_{T,j}^{\mathrm{NI}} u(\mathbf{x}_{T,j}^{\mathrm{NI}}) \qquad \text{with } N_{\mathrm{vol}} := \dim(\mathbb{P}_q(T)) = \frac{(q+1)(q+2)}{2} \text{ quadrature points} \tag{36}$$

that is exact for $u \in \mathbb{P}_q(T)$. Here NI stands for "Numerical Integration", and for simplicity the dependence of N_{vol}, $w_{T,j}^{\mathrm{NI}}$ and $\mathbf{x}_{T,j}^{\mathrm{NI}}$ on q has been made implicit.

One advantage of the Fekete points is that in the "volume" quadrature (36), a subset of the quadrature points belong to the edges of T where they coincide with the Gauss-Lobatto points,

hence providing quadrature formulas for the edges. In other words, on every edge $e \in \mathcal{E}(T)$ we have a quadrature formula

$$\int_e u \approx \sum_{j=1}^{N_{\mathrm{edge}}} w_{e,j}^{\mathrm{NI}} u(\mathbf{x}_{e,j}^{\mathrm{NI}}) \tag{37}$$

that is such that

$$\{\mathbf{x}_{e,j}^{\mathrm{NI}} : j = 1, \dots, N_{\mathrm{edge}}\} \subset \{\mathbf{x}_{T,j}^{\mathrm{NI}} : j = 1, \dots, N_{\mathrm{vol}}\} \qquad \text{for all } \ e \in \mathcal{E}(T). \tag{38}$$

Moreover, the edge quadrature (37) involves $N_{\mathrm{edge}} := q+1$ Gauss-Lobatto points, hence it is exact for $u|_e \in \mathbb{P}_{2q-1}(e)$. Equipped with these quadrature formulas we let the discrete current density in (27) be defined by $\tilde{\mathbf{J}}^{n+1/2} := \big(\tilde{\sigma}_\gamma^\varepsilon(\boldsymbol{J}_h^{n+\frac{1}{2}})\big)_{\gamma \in \tilde{\Lambda}_h^\varepsilon}$ with

$$\boldsymbol{J}_h^{n+\frac{1}{2}} = \pi_h^{\mathrm{div,NI}}(\boldsymbol{J}_N^{n+\frac{1}{2}}) := \sum_{\lambda \in \Lambda_h^\varepsilon} \sigma_\lambda^{\varepsilon,\mathrm{NI}}(\boldsymbol{J}_N^{n+\frac{1}{2}}) \boldsymbol{\varphi}_\lambda^\varepsilon, \qquad \text{where} \tag{39}$$

$$\begin{cases} \sigma_{T,d,\alpha}^{\varepsilon,\mathrm{NI}}(\boldsymbol{J}^{n+\frac{1}{2}}) := |\mathbf{F}_T|^{-1} \sum_{j=1}^{N_{\mathrm{vol}}} w_{T,j}^{\mathrm{NI}} (\tilde{\mathbf{F}}_T^t \boldsymbol{J}_N^{n+\frac{1}{2}}(\mathbf{x}_{T,j}^{\mathrm{NI}}))_d \, \pi_{T,\alpha}(\mathbf{x}_{T,j}^{\mathrm{NI}}) & \text{for } \ T \in \mathcal{T}_h, \ d = 0,1, \ \alpha \in \Gamma_{p-2}^2 \\ \sigma_{e,\beta}^{\varepsilon,\mathrm{NI}}(\boldsymbol{J}^{n+\frac{1}{2}}) := \sum_{j=1}^{N_{\mathrm{edge}}} w_{e,j}^{\mathrm{NI}} (\boldsymbol{J}_N^{n+\frac{1}{2}}(\mathbf{x}_{e,j}^{\mathrm{NI}}) \cdot \boldsymbol{n}_e) \, \pi_{e,\beta}(\mathbf{x}_{e,j}^{\mathrm{NI}}) & \text{for } \ e \in \mathcal{E}_h, \ \beta \in \Gamma_{p-1}^1. \end{cases} \tag{40}$$

Using the inclusion (38) we then see that the Fekete point values of $\boldsymbol{J}_N^{n+1/2}$ computed for the volume degrees of freedom can be reused for the edge degrees of freedom.

Remark 2.1. *In practice we can choose the degree $q \in 3\mathbb{N}$ of the Fekete formulas so that the order of the resulting FEM scheme is preserved. Since* (13) *is formally a scheme of order p, this amounts to asking that the approximation $\pi_h^{\mathrm{div}} \boldsymbol{J} \approx \pi_h^{\mathrm{div,NI}} \boldsymbol{J}$ is exact for $\boldsymbol{J} \in P_{p-1}(\mathcal{T}_h)^2$. When applied to the edge quadratures this yields $2q-1 \geq 2p-2$ and for the volume quadratures it gives $q \geq 2p-3$. Thus, for $p \leq 3$ we can take $q = 3$.*

2.3 The current deposition algorithm

To compute $\boldsymbol{J}_h^{n+\frac{1}{2}}$ we need the point values $\boldsymbol{J}_N^{n+\frac{1}{2}}(\mathbf{x}_{T,j}^{\mathrm{NI}})$, $T \in \mathcal{T}_h$, $j = 1, \dots, N_{\mathrm{vol}}$ (see (39), (40) and the inclusion (38)). Consequently in view of (34) we have to compute elementary contributions of the form

$$C_{T,j}^{\mathrm{NI}}(k,n) := \int_{t_n}^{t_{n+1}} S_\epsilon(\mathbf{x}_{T,j}^{\mathrm{NI}} - \mathbf{x}_k(t)) \frac{\mathrm{d}t}{\Delta t}. \tag{41}$$

Using the piecewise affine structure of the particle trajectories, and writing for simplicity

$$\tilde{\mathbf{x}}_k(\tau) = \tilde{\mathbf{x}}_k(T,j,n;\tau) := \mathbf{x}_{T,j}^{\mathrm{NI}} - \mathbf{x}_k(t) = \mathbf{x}_{T,j}^{\mathrm{NI}} - \mathbf{x}_k^n - \tau \mathbf{v}_k^{n+\frac{1}{2}} \quad \text{for} \quad \tau := t - t_n \in [0, \Delta t],$$

the elementary particle contribution (41) can be computed exactly with the following procedure.

Algorithm 2.2 (Exact computation of the time-averaged elementary particle contribution $C_{T,j}^{\mathrm{NI}}(k,n)$)**.**

Let us write $(\tilde{x}_k, \tilde{y}_k) = \tilde{\mathbf{x}}_k$ the above k-th particle trajectory relative to the j-th Fekete point of T.

1. *Find the biggest intervals $[\tau_1^\star, \tau_2^\star]$ and $[\tau_3^\star, \tau_4^\star]$ such that $-\epsilon \leq \tilde{x}_k(\tau) \leq \epsilon$ on $[\tau_1^\star, \tau_2^\star]$ and $-\epsilon \leq \tilde{y}_k(\tau) \leq \epsilon$ on $[\tau_3^\star, \tau_4^\star]$. Then set $\tau_\star := \max(0, \tau_1^\star, \tau_3^\star)$, $\tau^\star := \min(\Delta t, \tau_2^\star, \tau_4^\star)$, and observe that we have*

$$C_{T,j}^{\mathrm{NI}}(k,n) = \int_{\tau_\star}^{\tau^\star} S_\epsilon^{1d}(\tilde{x}_k(\tau)) S_\epsilon^{1d}(\tilde{y}_k(\tau)) \frac{\mathrm{d}\tau}{\Delta t}.$$

2. *Noticing that $\tilde{x}_k(\tau)$ and $\tilde{y}_k(\tau)$ are affine on $[\tau_\star, \tau^\star]$ and that S_ϵ^{1d} is a polynomial function on $[-\epsilon, \epsilon]$ (see (35)), it is an easy game to compute an explicit formula for the primitive of $S_\epsilon^{1d}(\tilde{x}_k(\tau))S_\epsilon^{1d}(\tilde{y}_k(\tau))$.*

The discrete current $\boldsymbol{J}_h^{n+\frac{1}{2}}$ is then implemented with a loop over the particles. To each particle with index $k = 1, \dots, N$, we associate a current density

$$\boldsymbol{J}_k^{n+\frac{1}{2}} := q w_k \int_{t_n}^{t_{n+1}} \mathbf{v}_k^{n+1/2} S(\mathbf{x} - \mathbf{x}_k(t)) \frac{\mathrm{d}t}{\Delta t}$$

and we observe that the quadratures $C_{T,j}^{\mathrm{NI}}(k,n)$ computed in Algorithm 2.2 satisfy

$$q w_k C_{T,j}^{\mathrm{NI}}(k,n) \mathbf{v}_k^{n+1/2} = q w_k \int_{t_n}^{t_{n+1}} \mathbf{v}_k^{n+1/2} S(\mathbf{x}_{T,j}^{\mathrm{NI}} - \mathbf{x}_k(t)) \frac{\mathrm{d}t}{\Delta t} = \boldsymbol{J}_k^{n+\frac{1}{2}}(\mathbf{x}_{T,j}^{\mathrm{NI}}). \tag{42}$$

In particular, the particle's contribution to the projected current reads

$$\begin{aligned}
\pi_h^{\mathrm{div,NI}}(\boldsymbol{J}_k^{n+1/2}) &= \sum_{\lambda \in \Lambda_h^\varepsilon} \sigma_\lambda^{\varepsilon,\mathrm{NI}}(\boldsymbol{J}_k^{n+\frac{1}{2}}) \varphi_\lambda^\varepsilon \\
&= \sum_{T \in \mathcal{T}_h} \sum_{d=0,1} \sum_{\alpha \in \Gamma_{p-2}^2} \Big[|\mathbf{F}_T|^{-1} \sum_{j=1}^{N_{\mathrm{vol}}} w_{T,j}^{\mathrm{NI}} \pi_{T,\alpha}(\mathbf{x}_{T,j}^{\mathrm{NI}}) (\tilde{\mathbf{F}}_T^t \boldsymbol{J}_k^{n+\frac{1}{2}}(\mathbf{x}_{T,j}^{\mathrm{NI}}))_d \Big] \varphi_{T,d,\alpha}^\varepsilon \\
&\quad + \sum_{e \in \mathcal{E}_h} \sum_{\beta \in \Gamma_{p-1}^1} \Big[\sum_{j=1}^{N_{\mathrm{edge}}} w_{e,j}^{\mathrm{NI}} \pi_{e,\beta}(\mathbf{x}_{e,j}^{\mathrm{NI}}) (\boldsymbol{J}_k^{n+\frac{1}{2}}(\mathbf{x}_{e,j}^{\mathrm{NI}}) \cdot \boldsymbol{n}_e) \Big] \varphi_{e,\beta}^\varepsilon \\
&= q w_k \sum_{T \in \mathcal{T}_h} \sum_{d=0,1} \sum_{\alpha \in \Gamma_{p-2}^2} \Big[|\mathbf{F}_T|^{-1} \sum_{j=1}^{N_{\mathrm{vol}}} w_{T,j}^{\mathrm{NI}} C_{T,j}^{\mathrm{NI}}(k,n) \pi_{T,\alpha}(\mathbf{x}_{T,j}^{\mathrm{NI}}) (\tilde{\mathbf{F}}_T^t \mathbf{v}_k^{n+1/2})_d \Big] \varphi_{T,d,\alpha}^\varepsilon \\
&\quad + q w_k \sum_{e \in \mathcal{E}_h} \sum_{\beta \in \Gamma_{p-1}^1} \Big[\sum_{j=1}^{N_{\mathrm{edge}}} w_{e,j}^{\mathrm{NI}} C_{T,j'}^{\mathrm{NI}}(k,n) \pi_{e,\beta}(\mathbf{x}_{e,j}^{\mathrm{NI}}) (\mathbf{v}_k^{n+1/2} \cdot \boldsymbol{n}_e) \Big] \varphi_{e,\beta}^\varepsilon,
\end{aligned} \tag{43}$$

where $j' = j'(j)$ is such that $\mathbf{x}_{T,j'}^{\mathrm{NI}} = \mathbf{x}_{e,j}^{\mathrm{NI}}$, see (38). Specifically, we compute $\pi_h^{\mathrm{div,NI}}(\boldsymbol{J}_k^{n+1/2})$ with a call to the following recursive algorithm (starting from the cell T that contains $\mathbf{x}_k^n$).

Algorithm 2.3 (Recursive computation of the k-th particle contribution to $\boldsymbol{J}_h^{n+\frac{1}{2}}$)**.** *Given a cell T, and assuming that the contributions to the volume dofs of T have not been computed yet, proceed as follows.*

(a) For every quadrature point $\mathbf{x}_{T,j}^{\mathrm{NI}}$ on the cell, use Algorithm 2.2 to compute (and store) the elementary particle contributions $C_{T,j}^{\mathrm{NI}}(k,n)$.

(b) For $d = 0, 1$ and $\alpha \in \Gamma_{p-2}^2$, compute the contribution

$$\begin{aligned}
\sigma_{T,d,\alpha}^{\varepsilon,\mathrm{NI}}(\boldsymbol{J}_k^{n+\frac{1}{2}}) &= |\mathbf{F}_T|^{-1} \sum_{j=1}^{N_{\mathrm{vol}}} w_{T,j}^{\mathrm{NI}} \pi_{T,\alpha}(\mathbf{x}_{T,j}^{\mathrm{NI}}) (\tilde{\mathbf{F}}_T^t \boldsymbol{J}_k^{n+\frac{1}{2}}(\mathbf{x}_{T,j}^{\mathrm{NI}}))_d \\
&= q w_k |\mathbf{F}_T|^{-1} \sum_{j=1}^{N_{\mathrm{vol}}} w_{T,j}^{\mathrm{NI}} C_{T,j}^{\mathrm{NI}}(k,n) \pi_{T,\alpha}(\mathbf{x}_{T,j}^{\mathrm{NI}}) (\tilde{\mathbf{F}}_T^t \mathbf{v}_k^{n+1/2})_d
\end{aligned}$$

and add it to the Raviart-Thomas coefficient (T,d,α) of the deposited current $\pi_h^{\mathrm{div,NI}}(\boldsymbol{J}_k^{n+1/2})$.

(c) For $e \in \mathcal{E}(T)$: if the contributions to the edge dofs associated with e have not been computed yet, then for $\beta \in \Gamma^1_{p-1}$, compute the contribution

$$\sigma^{\varepsilon,\mathrm{NI}}_{e,\beta}(\boldsymbol{J}_k^{n+\frac{1}{2}}) = \sum_{j=1}^{N_{\mathrm{edge}}} w^{\mathrm{NI}}_{e,j}\pi_{e,\beta}(\mathbf{x}^{\mathrm{NI}}_{e,j})(\boldsymbol{J}_k^{n+\frac{1}{2}}(\mathbf{x}^{\mathrm{NI}}_{e,j})\cdot\boldsymbol{n}_e)$$
$$= qw_k \sum_{j=1}^{N_{\mathrm{edge}}} w^{\mathrm{NI}}_{e,j} C^{\mathrm{NI}}_{T,j'}(k,n)\pi_{e,\beta}(\mathbf{x}^{\mathrm{NI}}_{e,j})(\mathbf{v}_k^{n+1/2}\cdot\boldsymbol{n}_e)$$

(where $j' = j'(j)$ is such that $\mathbf{x}^{\mathrm{NI}}_{T,j'} = \mathbf{x}^{\mathrm{NI}}_{e,j}$, see (38)) and add it to the Raviart-Thomas coefficient (e,β) of the deposited current $\pi_h^{\mathrm{div},\mathrm{NI}}(\boldsymbol{J}_k^{n+1/2})$.

(d) For every cell T' sharing an edge with T, do: if T' intersects the support of the moving particle, that is the convex set $\Omega^S(k,n) := [-\epsilon,\epsilon]^2 + \{\mathbf{x}_k(t) : t \in [t_n, t_{n+1}]\}$, see Remark 2.4 below, and if the particle contributions to the volume dofs associated with T' have not been computed yet, then

- *recursively call Algorithm 2.3 with $T = T'$,*
- *otherwise do nothing (i.e., stop the recursion).*

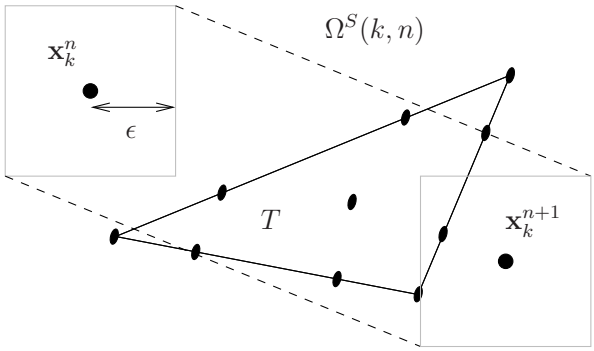

Figure 1: Example of a triangular mesh cell T (with its Fekete points for $q = 3$) intersecting the convex support $\Omega^S(k,n)$ of the k-th particle moving on the time step $[t_n, t_{n+1}]$.

Remark 2.4. *To test whether T intersects the convex set $\Omega^S(k,n) := [-\epsilon,\epsilon]^2 + \{\mathbf{x}_k(t) : t \in [t_n, t_{n+1}]\}$ (i.e., the moving particle support, see Figure 1), we can compute the determinants associated with the edges e_i^T of T, namely the set*

$$\left\{\det(\mathbf{x}^T_{i+2}-\mathbf{x}, \mathbf{x}^T_{i+1}-\mathbf{x}) \quad \textit{for} \quad \mathbf{x} \in \left\{\mathbf{x}_k^n + \epsilon\begin{pmatrix}\theta_x\\ \theta_y\end{pmatrix} + \tau\mathbf{v}_k^{n+1/2} :\ \theta_x,\theta_y \in \{-1,1\},\ \tau \in \{0,\Delta t\}\right\}\right\}.$$

If for some $i \in \{0,1,2\}$ these determinants are all positive (or zero), then the intersection has a zero measure and the particle k has no current contribution on the dofs associated to the cell T (nor to one of its edges). Otherwise, the intersection may have a positive measure.

3 A numerical study

3.1 An academic beam test case

To assess the performances of the above method we simulate an academic diode in a 2d domain $\Omega = [0, 0.1\text{m}]^2$. On the left boundary a beam of electrons is steadily injected and accelerated by a constant external field which derives from the electric potential imposed on both the cathode ($\phi_{\text{ext}} = 0$ on the left boundary) and the anode ($\phi_{\text{ext}} = 10^5\text{V}$ on the right boundary).

For simplicity, we consider that the beam is injected with a given distribution f_{inj} corresponding to a smooth space-density $n_{\text{inj}}(y)$ over the injection window $x = 0$, $y^-_{\text{inj}} := 0.03\text{m} \leq y \leq 0.07\text{m} =: y^+_{\text{inj}}$ and a Maxwellian distribution in the (first) velocity variable. Specifically, we consider

$$f_{\text{inj}}(t, \mathbf{x}, \mathbf{v}) := n_{\text{inj}}(y) M_{\text{inj}}(v_x) \delta_0(v_y) \quad \text{for} \quad \mathbf{x} \in \{0\} \times [y^-_{\text{inj}}, y^+_{\text{inj}}], \quad \mathbf{v} \in \mathbb{R}_+ \times \mathbb{R} \tag{44}$$

with

$$n_{\text{inj}}(y) := \frac{\bar{n}_{\text{inj}}\,\pi}{2} \sin\left(\frac{\pi(y - y^-_{\text{inj}})}{y^+_{\text{inj}} - y^-_{\text{inj}}}\right) \qquad \text{and} \qquad M_{\text{inj}}(v_x) := \frac{m_e}{2\pi \text{k} T_e} \exp\left(-\frac{m_e (v_x - v_{\text{inj}})^2}{2\text{k} T_e}\right).$$

Here the average injection speed is $v_{\text{inj}} := c/2$, and the kinetic electron temperature is such that the standard deviation in velocity is $\sigma = \sqrt{\text{k} T_e / m_e} = v_{\text{inj}}/10$. Finally we inject the electrons with an average current $\bar{J}_{\text{inj}} = q_e \bar{n}_{\text{inj}} v_{\text{inj}}$ of 10^4Am^{-2} (in absolute value), which determines the average density $\bar{n}_{\text{inj}}$. In Figure 2 we show the typical profile of the solution in the steady state regime, together with the mesh used in the test cases below.

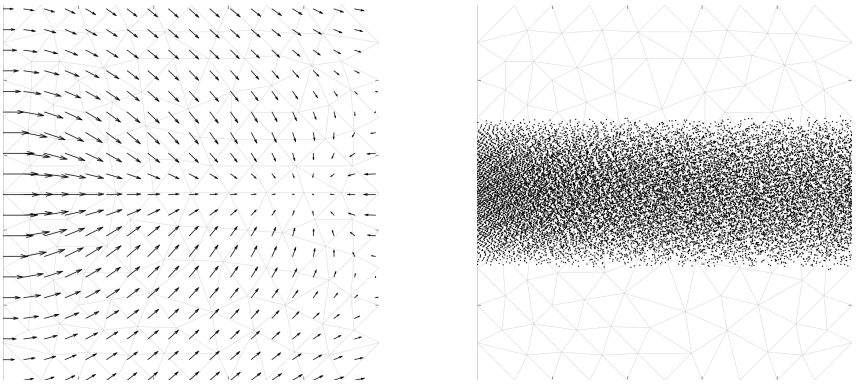

Figure 2: Academic beam test case. The self-consistent $\boldsymbol{E}$ field (left plot) and the numerical particles accelerated towards the right boundary (right plot) show the typical profile of the solution in the steady state regime. For the considered geometry the external field is constant $\boldsymbol{E}_{\text{ext}} = -10^6 \text{Vm}^{-1}$.

3.2 Charge-conserving injection of smooth particles

The above inflow distribution (44) is discretized by loading macro-particles (Dirac or smooth) on the discrete times $t_n = n\Delta t$, $n = 0, 1, \ldots$, as follows. To preserve the discrete Gauss law and to avoid a systematic approximation error on the injection boundary when finite-size particles are used, we load the particles in a virtual region outside the computational domain similarly as in other approaches, see e.g., [5] for the case of Dirac particles.

We first describe our injection procedure for the case of a single injection speed, say v_{inj}. Since the basic idea is to use a standard loading algorithm to approximate the injected beam before

it enters the domain, we extend the inflow space density n_{inj} uniformly for $x < 0$, and we load the particles in a portion of this virtual beam corresponding to $x \in [x^-_{\text{inj}}, x^+_{\text{inj}}]$. In order that no charge be loaded inside the computational domain, we take $x^+_{\text{inj}} := -\epsilon$ where we recall that ϵ is the radius of the particle shape support, see (35). Next, because particles in this virtual region are simply transported and feel no force, we see that (i) they will enter the computational domain with their loading velocity, and (ii) in order that the successive particle loadings correspond to a regular sampling of the injected beam, we must set

$$x^-_{\text{inj}} := x^+_{\text{inj}} - v_{\text{inj}} \Delta t. \tag{45}$$

Finally, if we want to inject particles with different speeds the above procedure can be modified by adapting the length of the virtual loading region according to the actual velocity of each particle. Specifically, the random position of a particle loaded with velocity $v_x = v^0_k$ should be drawn on a virtual region $[x^-_{\text{inj},k}, x^+_{\text{inj}}]$ corresponding to

$$x^+_{\text{inj}} := -\epsilon \qquad x^-_{\text{inj},k} = x^-_{\text{inj}}(v^0_k) := x^+_{\text{inj}} - v^0_k \Delta t \tag{46}$$

as depicted in Figure 3.

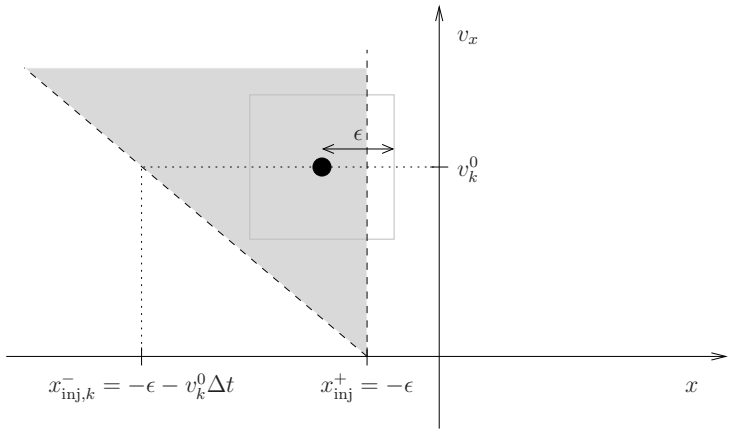

Figure 3: Phase-space profile of the smooth particle injection. For a charge-conserving injection, particles must be loaded at each time step in a "virtual" region (outside the computational domain $x \geq 0$) where the inflow distribution f_{inj} is extended uniformly with respect to $x < 0$. For an accurate discretization with smooth shapes of radius ϵ, particles with an initial speed of $v_x = v^0_k$ must then be loaded following this virtually extended distribution on an interval $[-\epsilon - v^0_k \Delta t, -\epsilon]$.

3.3 Numerical results

In Figures 4 and 5 we show the results obtained with the above finite element scheme (13) coupled with the tensor-product Jacobs-Hesthaven particles (35) and we compare them with two standard mixed finite element schemes coupled with point particles. The key is as follows.

- All the curves display the relative error $\|F_h - F_{\text{ref}}\|/\|F_{\text{ref}}\|$ of some numerical field F_h versus the cpu time of the associated run. Here the considered fields are either the projected current density $\boldsymbol{J}_h = \pi^{\text{div},NI}_h \boldsymbol{J}$ (plots in the top rows), the finite element electric field $\boldsymbol{E}_h$ (in the center rows) or the finite element magnetic field B_h (in the bottom rows), and the errors are measured in L^2 (left plots) and L^∞ (right plots).

- All the finite element schemes use the same mesh (an unstructured triangulation of the domain $\Omega = [0, 0.1]^2$ using 244 triangles with maximum diameter $h \approx 0.016$) and the same time domain, chosen so that particles have travelled approximatively three diode lengths before the final time step where errors are measured. As for the reference fields, they were obtained using a fine mesh of 2158 triangles with maximum diameter $h \approx 0.005$, and smooth particles.

- Abscissas show the cpu times in seconds, each simulation being run on a 2.3 GHz Intel Core i7 laptop. Because depositing the current is the most expensive part, the runs were sped-up by a parallel treatment of the particles using 7 processes.

- Curves with dashed lines show results obtained with the "strong-Ampère" mixed finite-element method described (13) coupled with the smooth tensor-product particles (35). Each curve corresponds to a different ratio between the particle radius $\epsilon > 0$ and the mesh resolution h (defined as the maximum diameter of the triangles in the mesh), as indicated in the plots.

- Curves with solid lines show results obtained with point particles ($\epsilon = 0$, that is $S = \delta$) for comparison, coupled with two different finite-element Maxwell solvers. The filled circles correspond to point particles coupled with the "strong-Ampère" finite-element scheme (13) and the empty circles correspond to point particles coupled with the standard "strong-Faraday" mixed finite-element scheme (17).

- In each curve, the different points correspond to different numbers N_{ppc} of particles per cell. This number determines the number of particles loaded in the virtual region outside the computational domain as described in Section 3.2. It is indicated in the point particles runs (where it varies between 50 and 5000) but has been ommited for readibility in the smooth particle runs, where it varies between 5 and 50. Note that here the beam propagates on a region containing approximatively 90 triangular cells, so that in the steady-state regime the number of particles that are pushed at each time step in the computational domain is of about $90N_{\text{ppc}}$.

Observing first the convergence curves obtained with point particles (solid lines with circle points) we point out two facts.

- First, the "strong-Ampère" runs are much faster than the "strong-Faraday" ones. One reason for this is that in the latter runs one must solve at each time step a linear problem involving the mass matrix of the curl-conforming finite element space used for the electric field. In the "strong-Ampère" runs the linear problems to be solved involve the mass matrix of the continuous elements space for the magnetic field, which is much smaller since B is scalar valued. A second reason is that point particles deposit their current with less operations in the "strong-Ampère" scheme than in "strong-Faraday" schemes.

- Second, the "strong-Faraday" finite element scheme appears to be more robust than the "strong-Ampère" one, indeed with the latter we observe spurious results for some values of N_{ppc}. This may be caused by the fact that when extended to point particles, $\pi_h^{\text{div}} \boldsymbol{J}_N^{n+1/2}$ is not a continuous function of the particle positions. Indeed, when a particle k moves exactly along a mesh edge this projection involves volume-based degrees of freedom of $\boldsymbol{J}_k^{n+1/2}$ which are essentially products between a Dirac measure on an edge and a piecewise polynomial function that is fully discontinuous there. This effect does not appear when the particles deposit their current in the curl-conforming finite element space involved in the "strong-Faraday" scheme, as explained in [2, Lemma 3.1].

From the convergence curves displayed in Figures 4 and 5 we then draw the following observations.

- Among the parameters for which different values are taken in our tests (i.e., the number of particles per cell N_{ppc}, the ratio ϵ/h and the degree of the smooth particle shape), the most critical one seems to be the ratio between the particle radius ϵ and the maximum diameter h of the mesh cells. Specifically, our results indicate that the best results (in terms of accuracy and computational time) are obtained for smooth particles with radius ϵ in an approximate range of $h/4$ to $h/2$, and for particles shapes (35) with coordinate degree $2a = 4$, the latter value seems to be the best choice for all the measured errors. Note that since h is the maximum *diameter* of the mesh cells, this amounts to taking smooth particles with approximatively the same diameter as the mesh cells.

- For the parameters chosen here, increasing the coordinate degree of the particles from $2a = 2$ to $2a = 4$ slightly improves the accuracy of the runs with particles radius of $\epsilon \geq h/2$ and it deteriorates those with $\epsilon \leq h/4$. It has no significant effect on the computational time.

- Increasing the number N_{ppc} of particles per cell improves the numerical accuracy for small particles ($\epsilon \leq h/4$) but has basically no impact for medium or large particles ($\epsilon \geq h/2$). On the other hand, it always deteriorates the cpu time of the runs.

- The best compromise between numerical accuracy and computational time seems to be obtained for smooth particles with coordinate degree of $2a = 4$ and radius $\epsilon \approx h/2$ (i.e., particles with about the same diameter as the mesh cells), when using $N_{\text{ppc}} \approx 5 - 10$ particles per cell. With those parameters the computational time is about the same as when using the "strong-Ampère" finite element solver with about 200 point particles per cell, and the numerical accuracy is improved by a factor ranging from approximatively 2 (when measured in L^2) to more than 4 (when measured in L^∞).

Finally, we show in Figure 6 the snapshots of the electro-magnetic fields corresponding to the "strong-Ampère" finite-element scheme coupled with about 200 point particles per cell (left plots) and about 5 smooth particles per cell (right plots), with the parameters described just above. As seen in Figure 5 these two runs took about the same cpu time (14 seconds), which clearly demonstrates the higher efficiency of the smooth particles for this test case.

Conclusion

In this work we have proposed a conforming finite-element scheme for the 2d time-dependent Maxwell system that preserves a strong Gauss law when the current is deposited from the particles with a Raviart-Thomas finite-element interpolation, and we have described an algorithm based on Fekete quadrature formulas for computing a numerical approximation of this current when the particles have a smooth shape. A numerical study involving an academic beam test-case with smooth injected current is used to assess the performances of the coupled scheme, and it is shown that with a non-optimized implementation the proposed method is more accurate than two finite-element schemes using point (Dirac) particles, for an appropriate choice of the particle parameters.

References

[1] D. Boffi, F. Brezzi, and M. Fortin. *Mixed finite element methods and applications*, volume 44 of *Springer Series in Computational Mathematics*. Springer, 2013.

[2] M. Campos Pinto, S. Jund, S. Salmon, and E. Sonnendrücker. Charge conserving fem-pic schemes on general grids. *C.R. Mécanique*, 342(10-11):570–582, 2014.

[3] V. Girault and P.-A. Raviart. *Finite Element Methods for Navier-Stokes Equations – Theory and Algorithms*. Springer Series in Computational Mathematics. Springer-Verlag, Berlin, 1986.

[4] G.B. Jacobs and J.S. Hesthaven. High-order nodal discontinuous Galerkin particle-in-cell method on unstructured grids. *Journal of Computational Physics*, 214(1):96–121, May 2006.

[5] J. Loverich, C. Nieter, D. Smithe, S. Mahalingam, and P. Stoltz. Charge conserving emission from conformal boundaries in electromagnetic PIC simulations. Unpublished (2010).

[6] P. Monk. A mixed method for approximating Maxwell's equations. *SIAM Journal on Numerical Analysis*, pages 1610–1634, 1991.

[7] M.L. Stowell and D.A. White. Discretizing transient current densities in the maxwell equations. In *ICAP 2009*, 2009.

[8] M.A. Taylor, B.A. Wingate, and R.E. Vincent. An algorithm for computing Fekete points in the triangle. *SIAM Journal on Numerical Analysis*, 38(5):1707–1720, 2000.

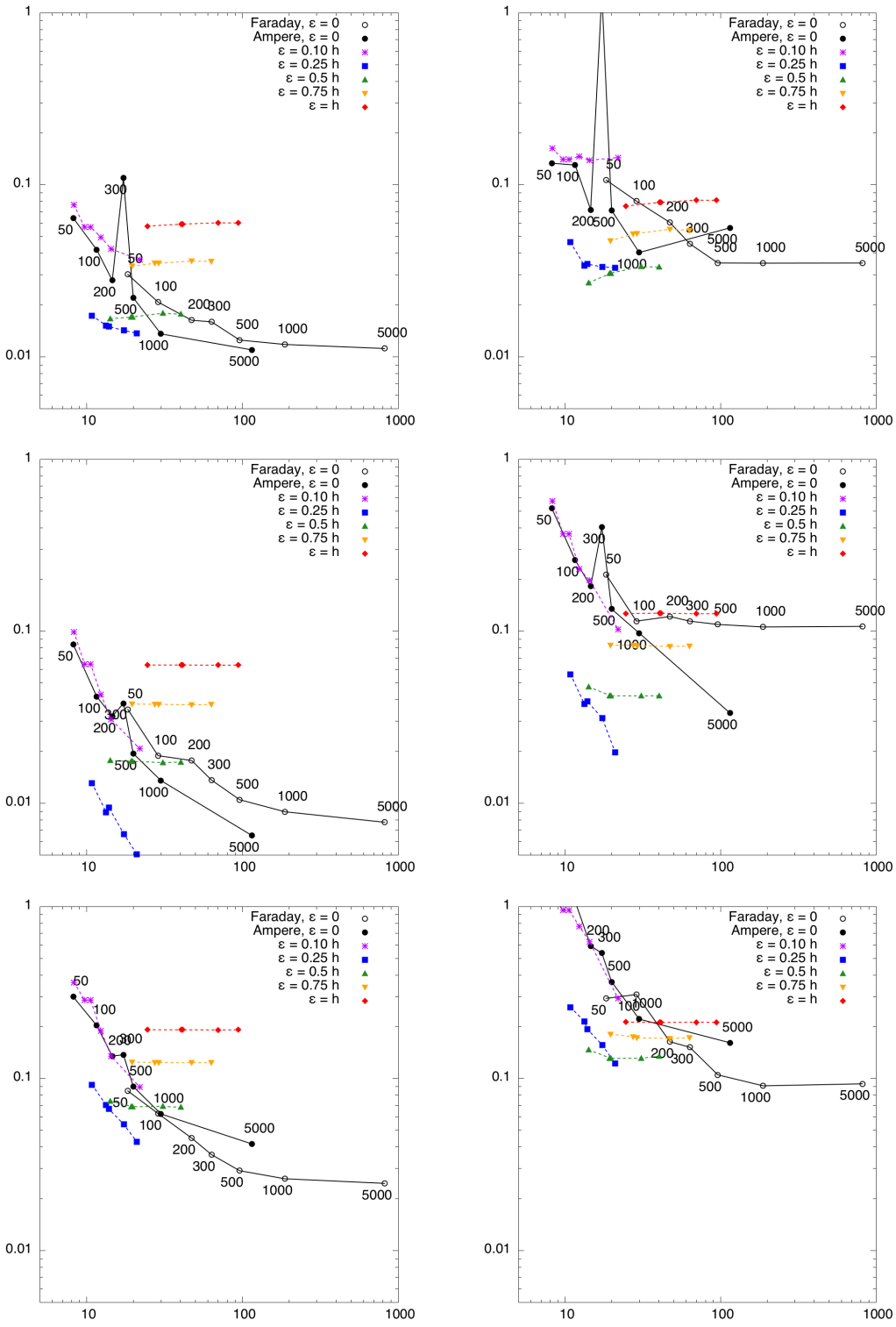

Figure 4: Relative error curves obtained with tensor-product Jacobs-Hesthaven particles of coordinate degree $2a = 2$ and different values for the particle radius $\epsilon > 0$. Filled and empty circles (black curves) correspond to simulations using point particles ($\epsilon = 0$), see the text for details. Here the errors are measured in L^2 (left) and L^∞ (right) for the current density $\boldsymbol{J}$ (top), the electric field $\boldsymbol{E}$ (center) and the magnetic field B (bottom). The abscissa shows the respective cpu times.

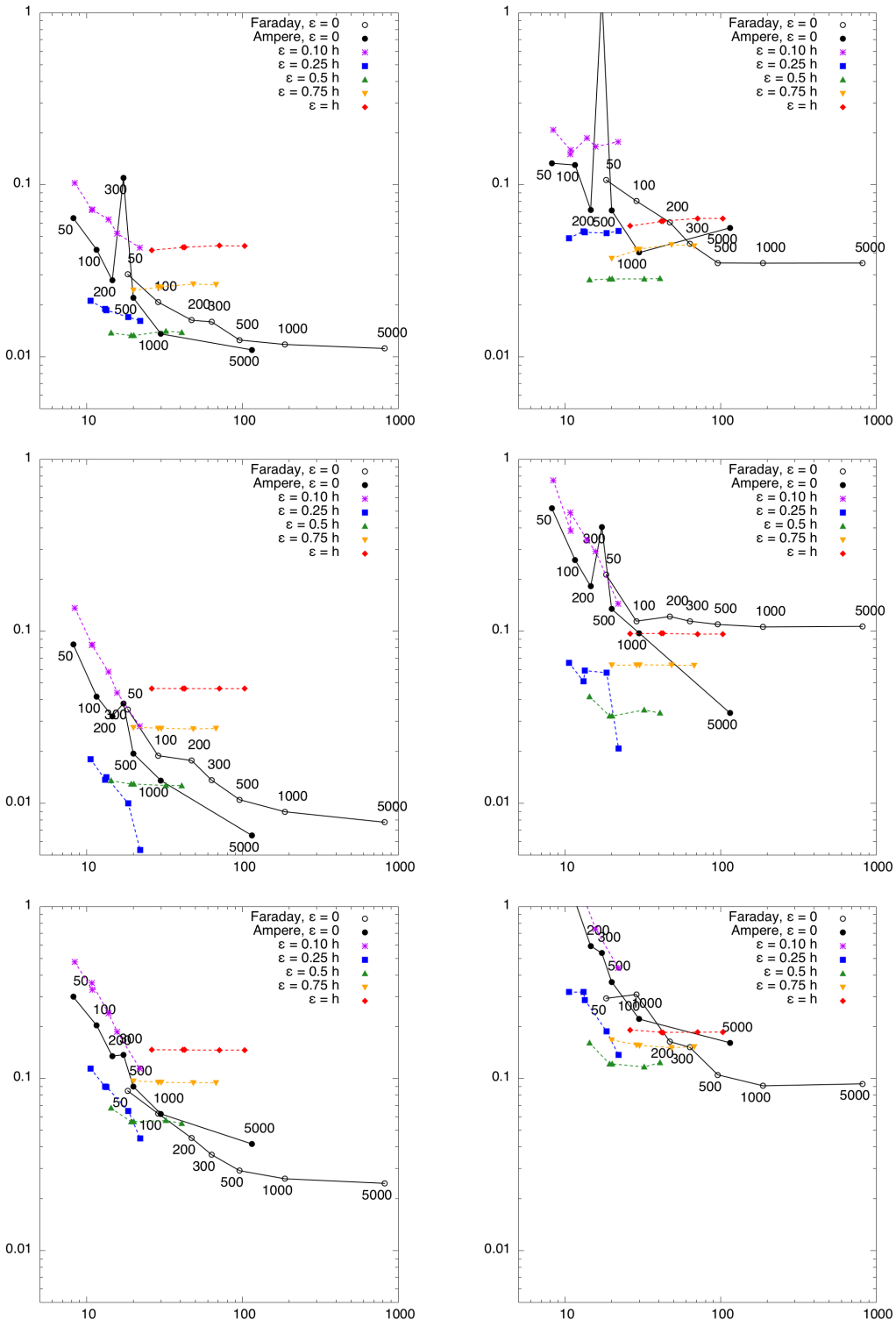

Figure 5: Relative error curves obtained with tensor-product Jacobs-Hesthaven particles of coordinate degree $2a = 4$ and different values for the particle radius $\epsilon > 0$. Filled and empty circles (black curves) correspond to simulations using point particles ($\epsilon = 0$), see the text for details. Here the errors are measured in L^2 (left) and L^∞ (right) for the current density $\boldsymbol{J}$ (top), the electric field $\boldsymbol{E}$ (center) and the magnetic field B (bottom). The abscissa shows the respective cpu times.

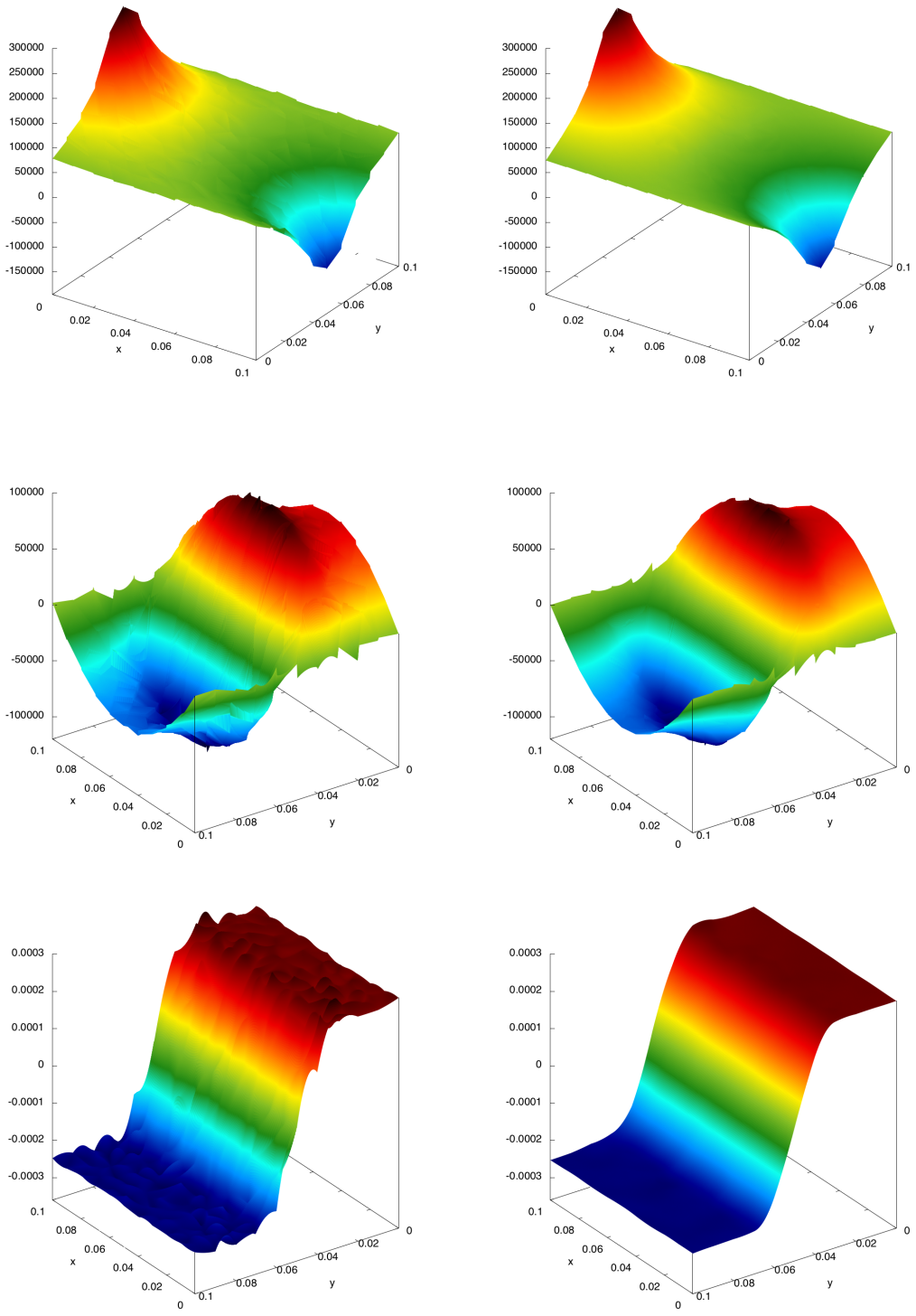

Figure 6: Academic beam test-case. Snapshots of the self-consistent fields (E_x on the top row, E_y on the center row and B on the bottom row) obtained with the "strong-Ampère" mixed finite-element scheme (13) coupled with smooth particles (left plots) and smooth Jacobs-Hesthaven particles (35) of radius $\epsilon = h/2$ (right plots) with respective numbers N_{ppc} of particles per cell of about 200 and 5. For these two runs the cpu time was the same, namely 14 seconds.